Sensitivity analysis of the numerical study on the thermal performance of a packed-bed molten salt thermocline thermal storage system

Chao Xu [a,*], Zhifeng Wang [a], Yaling He [b], Xin Li [a], Fengwu Bai [a]

[a] Key Laboratory of Solar Thermal Energy and Photovoltaic System, Institute of Electrical Engineering, Chinese Academy of Sciences, Beijing 100190, China
[b] Key Laboratory of Thermo-Fluid Science and Engineering of MOE, School of Energy and Power Engineering, Xi'an Jiaotong University, Xi'an, Shaanxi 710049, China

ARTICLE INFO

ABSTRACT

In this paper, a comprehensive transient, two-dimensional, two-phase model for heat transfer and fluid dynamics within the packed-bed molten salt thermocline thermal storage system is presented. After model validation, the developed model is used to investigate the general thermal behavior of a discharging process of the pack-bed thermocline system and evaluate the interstitial heat transfer coefficient, the effective thermal conductivity and effect of the thermal conductivity of solid fillers. The results show that the thermocline region is moving upward with slight expansion during the discharging process. With the use of two insulation layers, a uniform cross-sectional temperature distribution is well achieved. The use of different correlations for the interstitial heat transfer coefficient or the effective thermal conductivity from the literature leads to negligible difference in the predicted thermal performance. It is also found that decreasing the heat transfer rate between fluid and solid fillers, or increasing the thermal conductivity of solid fillers, results in an increase in the thermocline thickness which finally decreases the effective discharging time and the effective discharging efficiency.

© 2011 Elsevier Ltd. All rights reserved.

1. Introduction

Concentrating solar power (CSP) technologies which utilize inexhaustible and clean solar energy have been projected as one of the most promising candidates for substituting conventional power generation technologies [1–5]. Recently, rapid development occurred worldwide in basic technology and market strategy for CSP technologies including parabolic trough, power tower and dish/engine. However, as with most renewable energy systems, sunlight is available only in daylight hours which even in the best case is less than 50%, and it is still heavily influenced by clouds, aerosols, etc. To increase the availability beyond normal daylight hours, a thermal energy storage (TES) system which stores solar thermal energy for later use is usually incorporated in the CSP system. The TES system is a key performance advantage of the CSP technology, and it can significantly increase the hours of electricity generation and improve the dispatchability of CSP plants. Also, a low-cost TES system helps to reduce the levelized cost of electricity (LCOE) for CSP systems.

Different TES systems have been proposed and implemented in the past: oil, solid substances, saturated water and molten salt. Of these systems, molten salt offers the best balance of capacity, cost, efficiency and usability at high temperatures. Presently, TES

systems using molten salt are widely implemented or under development worldwide [6–12]. The molten salt TES systems can be generally categorized into two-tank system and one-tank thermocline system. The two-tank system has two tanks for storing the molten salt: one at high temperature and the other at low temperature. The two-tank molten salt system is the most proven utility-scale TES system, and it has been used or projected in many CSP plants including the 10 MW Solar Two tower plant in America, the Andasol (1-3) parabolic trough power plant (50 MW per plant) in Spain and the 280 MW Solana parabolic trough power plant in America [7,8,13].

The one-tank system only has one storage tank, within which a portion of the medium is at high temperature and a portion is at low temperature. The high- and low-temperature regions are separated by a temperature gradient or thermocline. During the charging process, high-temperature fluid from the solar receiver enters the top of the tank and exits the bottom at low temperature. Accordingly, the thermocline moves downward and thermal energy is stored in the high-temperature region. During the discharging process, the molten salt flows reversely and the thermocline moves upward. Compared to the two-tank system, the one-tank thermocline system requires only one storage tank, and low-cost solid storage medium can be used in the tank to replace part of the molten salt (referred to packed-bed thermocline), which can effectively reduces the cost of TES system by 20–37% [6]. Due to the benefit of low cost, the packed-bed thermocline system has

* Corresponding author. Tel.: +86 10 82547036; fax: +86 10 62587946.
E-mail address: mechxu@gmail.com (C. Xu).

Nomenclature

C_F	inertial coefficient		
c_p	specific heat capacity, $\mathrm{J\,kg^{-1}\,T^{-1}}$		
D	diameter of the storage tank, m		
d_p	diameter of the particle filler, m		
g	acceleration due to gravity, $\mathrm{m\,s^{-2}}$		
H	tank height, m		
h_v	interstitial heat transfer coefficient, $\mathrm{W\,m^{-3}\,K^{-1}}$		
K	permeability of porous material, $\mathrm{m^2}$		
k	thermal conductivity, $\mathrm{W\,m^{-1}\,K^{-1}}$		
L	length, m		
$\dot{m}$	mass flow rate, $\mathrm{kg\,s^{-1}}$		
Nu	Nusselt number		
p	pressure, Pa		
Pr	Prandtl number		
Re	Reynolds number		
r	radius, m		
T	temperature, K		
t	time, s		
V	tank volume, $\mathrm{m^3}$		
u	velocity, $\mathrm{m\,s^{-1}}$		
x	location along the axis of the tank, m		

Greek

ε porosity of packed-bed region
η efficiency
μ viscosity, $\mathrm{kg\,m^{-1}\,s^{-1}}$
Γ effective thermal conductivity, $\mathrm{W\,m^{-1}\,K^{-1}}$
ρ density, $\mathrm{kg\,m^{-3}}$

Subscripts

crit   critical value
d   discharging
eff   effective value
h   hot fluid
i   insulation layer 1, tank steel wall, and insulation layer 2
in   inlet
in1   insulation layer 1
in2   insulation layer 2
l   liquid molten salt; cold fluid
ms   molten salt
out   outlet
s   solid fillers
st   stainless steel

attracted more and more attention. A small pilot-scale (2.3 MWh t) packed-bed molten salt thermocline system has been successfully demonstrated in Sandia National Laboratories [11]. Quartzite rocks and sands were chosen as the low-cost solid fillers which provided the bulk of thermal capacitance of the thermal storage [14]. Zuo and Li [15] developed a molten salt thermocline system combining with two storage subsystems using phase change materials at the top and bottom of the tank.

However, large-scale utilization of the packed-bed thermocline system is still hindered by several technical problems. For instance, the thermocline region is prone to expanding with time or degrading after several charging–discharging cycles. To overcome these problems, it is essential to gain a comprehensive understanding about the operation process of the system and the related inherent-coupled heat and mass transport mechanisms. Since many important parameters are associated with the development process of this system, numerical investigations have been needed to minimize the expensive and time-consuming experimental investigations.

Although great efforts have been focused on the numerical investigations of thermal performance of the packed-bed thermocline system using water or oil as the fluid [16–25], little work has been reported about the numerical investigations of the packed-bed molten salt thermocline system [6,25–28]. Pacheco et al. [26] carried out a simple numerical investigation of the thermal behavior of the packed-bed molten salt thermocline system. The one-dimensional Schumann equations which involved several assumptions and simplifications were used in the modeling of heat transport between molten salt and solid fillers. Researchers in the National Renewable Energy Laboratory (NREL) [6] numerically modeled the packed-bed molten salt thermocline system in which the solid fillers were in the form of hexagonal rods or a honeycomb-like structure. Adiabatic boundary conditions were adopted when studying the core region of the tank. Yang and Garimella [27,28] developed a comprehensive two-temperature model to systematically investigate the discharging behavior of a packed-bed molten salt thermocline system. The effects of several parameters including tank height, molten-salt flow rate, and filler particle size on the thermal behavior were investigated. The effects of heat losses to the ambient air were also explored by employing non-adi-

abatic thermal boundary conditions with different heat transfer coefficients. Most recently, Lew et al. [25] numerically investigated the packed-bed thermocline system using the modified one-dimensional Schumann equations. Design procedures of the system were also discussed using the numerical modeling tool.

From the literature review, it can be seen that previous numerical investigations lack in a clear knowledge about the following two aspects: (1) the effects of some transport mechanisms, e.g., the two-dimensional thermal conduction between solid particles, have not been fully understood due to model simplifications; (2) various important constitutive correlations from the literature, e.g., the interstitial heat transfer coefficient between molten salt and solid fillers and the effective thermal conductivities of molten salt and solid fillers, have not been evaluated. Accordingly, this study aims at developing a comprehensive transient, two-dimensional, two-phase model for the packed-bed molten salt thermocline system with evaluations on various transport mechanisms and constitutive correlations. The rest of the paper is organized as follows. The transient two-dimensional two-phase model formulation for heat transfer and fluid dynamics within the packed-bed thermocline system will be first presented, and various constitutive correlations in the literature will be summarized. Then, the developed model will be validated based on the experimental results in the literature. The results and discussion will be shown for various aspects including the general thermal behavior, evaluations on the interstitial heat transfer coefficient and the effective thermal conductivity, and the effect of the thermal conductivity of solid fillers. Finally, some conclusions will be given.

2. Present model description

2.1. Governing equations

The general layout of the thermocline storage system is illustrated in Fig. 1a, which is similar to Yang et al.'s work [27–29]. As can be seen, the thermocline storage system mainly composes of a vertically standing cylindrical tank and the contained storage material, i.e., the molten salt and solid fillers. The tank has inlet/exit ports on the top and bottom for the flow of hot and cold molten salt,
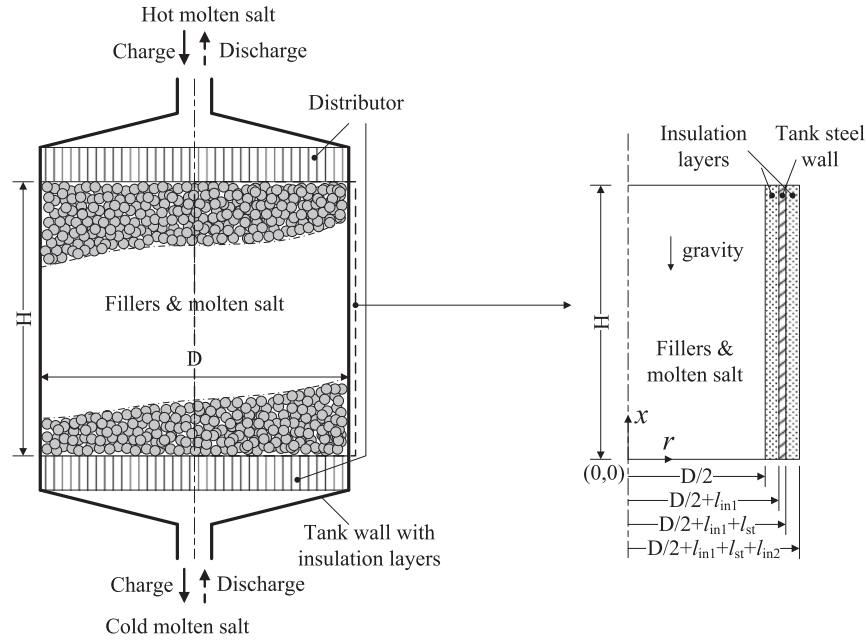
Fig. 1. Schematic diagram of the packed-bed molten salt thermocline TES and the computational domain.

respectively. Adjacent to the two exits, there are usually two short distributors which are sophisticated-designed to uniformly distribute flow of molten salt through the whole cross section of the packed-bed region. The pack-bed region which is the thermal storage region and composes of solid fillers and molten salt takes up the bulk of the tank volume. Due to the occupancy of the solid fillers, the molten salt only takes up a void fraction of the original thermal storage volume. This void fraction is defined as $\varepsilon = V_{ms}/V_{tank}$. During the charging process, the hot molten salt heated from the solar receiver system enters the storage tank from the upper port, transfers heat to the cold solid fillers, and leaves the tank through the bottom port with a lower temperature. As thus, solar thermal energy from the receiver system is stored in the cylindrical tank. Reversely, during the discharging process, the cold molten salt enters the tank from the bottom port and gets heated by the hot solid fillers in the storage system out of which it emerges as hot molten salt.

In the following, we present a transient, two-dimensional, two-phase model to formulate the heat transfer and fluid dynamics within the packed-bed thermocline storage tank. Since the molten salt and solid fillers may be at different temperatures due to the convective heat transfer process between them, the energy equations are applied separately to the two phases. The model is based on the following assumptions to simplify the analysis:

  (i) The fluid flow and heat transfer is symmetrical about the axis. Therefore, the governing equations for transport within the storage tank become two-dimensional.
 (ii) No distributors are included in the computational domain and a uniform flow is imposed at the inlet and outlet of the filler region, since that is thermally equivalent to a storage tank with well designed distributors [28].
(iii) The solid fillers behave as a continuous, homogeneous, and isotropic porous medium, and not as a medium composed of independent particles.
 (iv) The flow of molten salt through the packed-bed region is laminar and incompressible.
  (v) The properties of the solid fillers are constant.

With the above assumptions, the transient two-dimensional two-phase governing equations for the heat transfer and fluid

dynamics based on the computational domain shown in Fig. 1b can be given as follows.

- Continuity equation:

$$\frac{\partial(\varepsilon \rho_l)}{\partial t} + \nabla \cdot [\rho_l \vec{u}] = 0 \tag{1}$$

where ρ_l is the density of molten salt, ε is the porosity of the packed-bed structure, and $\vec{u} = u_r \vec{e}_r + u_x \vec{e}_x$ represents the superficial velocity vector based on the total cross-sectional area of the fluid and porous medium.

- Momentum equation:

$$\frac{\partial(\rho_l \vec{u})}{\partial(\varepsilon t)} + \frac{\nabla \cdot [\rho_l \vec{u} \vec{u}]}{\varepsilon^2} = \nabla \cdot (\mu \nabla \vec{u}) - \nabla p + \rho_l \vec{g} - \left(\frac{\mu}{K} + \frac{C_F \rho}{\sqrt{K}} |\vec{u}|\right) \vec{u} \tag{2}$$

where K is the intrinsic permeability of the porous medium, μ is the viscosity of molten salt, and C_F is the inertial coefficient.

- Energy equation for the molten salt:

$$\frac{\partial(\varepsilon \rho_l c_{p,l} T_l)}{\partial t} + \nabla \cdot [\rho_l c_{p,l} \vec{u} T_l] = \nabla \cdot (\Gamma_{l,eff} \nabla T_l) + h_v (T_s - T_l) \tag{3}$$

where T_l and T_s represent the temperatures of molten salt and solid fillers, respectively, $c_{p,l}$ is the specific heat capacity of molten salt, $\Gamma_{l,eff}$ is the effective thermal conductivity of molten salt, and the last term on the right side accounts for the heat transfer between the molten salt and solid fillers with a volumetric interstitial heat transfer coefficient h_v.

- Energy equation for the solid fillers:

$$\frac{\partial((1-\varepsilon)\rho_s c_{p,s} T_s)}{\partial t} = \nabla \cdot (\Gamma_{s,eff} \nabla T_s) - h_v (T_s - T_l) \tag{4}$$

where $c_{p,s}$ is the specific heat capacity of filler material and $\Gamma_{s,eff}$ is the effective thermal conductivity of solid fillers.

From Eqs. (3) and (4), it should be noted that the interstitial heat transfer coefficient couples the energy conservation equations of molten salt and solid fillers, and thus it seems crucial for the thermal performance of the packed-bed system.

- Energy equation for the insulation layers and tank steel wall:

$$\frac{\partial(\rho_i c_{p,i} T_i)}{\partial t} = \nabla \cdot (\Gamma_i \nabla T_i) \tag{5}$$

where i means insulation layer 1, tank steel wall, and insulation layer 2. It should be mentioned that the two-layer insulation structure of the present study is adopted from [29].

2.2. Material properties and constitutive correlations

The thermo-physical properties of molten salt (i.e., a mixture of 60 wt% NaNO$_3$ and 40 wt% KNO$_3$) change with temperature and can be found as follows [30]:

Density, $\rho(\text{kg/m}^3) = 2090 - 0.636 \times T(°C)$ (6)

Specific heat, $c_p(\text{J/(kg K)}) = 1443 - 0.172 \times T(°C)$ (7)

Thermal conductivity, $k(\text{W/(mk)})$
$$= 0.443 + 1.9 \times 10^{-4} \times T(°C) \tag{8}$$

Viscosity : $\mu(\text{kg/(ms)})$
$$= [22.714 - 0.12 \times T(°C) + 2.281 \times 10^{-4} \times T(°C)^2$$
$$- 1.474 \times 10^{-7} \times T(°C)^3] \times 10^{-3} \tag{9}$$

While for the solid fillers, the properties are treated as constants and depend on the used material. For instance, for the quartzite rock as solid fillers, it has a density of 2500 kg m^{-3}, specific heat capacity of 830 J kg^{-1}K^{-1}, and thermal conductivity of 5.69 W m^{-1}K^{-1}.

The permeability and inertial coefficient of the porous structure can be expressed as [31]:

$$K = \frac{d_p^2 \varepsilon^3}{150(1-\varepsilon)^2} \tag{10}$$

$$C_F = \frac{1.75}{\sqrt{150\varepsilon^3}} \tag{11}$$

where d_p is the diameter of the particle filler.

The interstitial heat transfer coefficient between the molten salt and solid fillers, h_v, and the effective thermal conductivities of molten salt and solid fillers, $\Gamma_{l,eff}$ and $\Gamma_{s,eff}$, are of great importance to evaluate the overall performance of the packed bed system. Various correlations have been developed based on experimental results and have been used in numerical models, which are summarized in Tables 1 and 2 for the interstitial heat transfer coefficient and the effective thermal conductivity, respectively. The correlations in Tables 1 and 2 are also shown as curves in Fig. 2. However, little information has been revealed about the difference between these correlations and the effect of using different correlations on the predicted performance. In this work, all the correlations listed in Tables 1 and 2 are tested to make an evaluation

about them. In Tables 1 and 2, the related Nusselt number, Prandtl number, and Reynolds number are given as below:

$$\text{Nu}_p = \frac{h_v d_p^2}{k_f}; \quad \text{Pr} = \frac{c_{pf} \mu}{k_f}; \quad \text{Re}_p = \frac{\rho_f d_p |\vec{u}|}{\mu} \tag{12}$$

2.3. Boundary conditions and initial conditions

As mentioned above, the present study focuses on the discharging process of the storage system. Thus, the boundary conditions (BCs) and initial conditions are given for the discharging process as described below.

2.3.1. Boundary conditions
2.3.1.1. BC 1 (x = 0, 0 ⩽ r < D/2). This boundary represents the inlet of cold molten salt, at which the temperature and velocity of molten salt are specified to be inlet conditions. For the temperature of solid fillers, the adiabatic condition is employed:

$$u|_+ = u_{in}, \quad v|_+ = 0, \quad T_f|_+ = T_{inf}, \quad \partial T_s/\partial x|_+ = 0 \tag{13}$$

2.3.1.2. BC 2 (x = H, 0 ⩽ r < D/2). This boundary represents the outlet of hot molten salt, at which the boundary conditions are given as follow:

$$\partial u/\partial x|_- = 0, \quad v|_- = 0, \quad \partial T_f/\partial x|_- = 0, \quad \partial T_s/\partial x|_- = 0 \tag{14}$$

2.3.1.3. BC 3 (0 ⩽ x ⩽ H, r = 0). This boundary represents the symmetry axis of the cylindrical tank, at which symmetrical boundary conditions are employed to the fluid and solid fillers temperatures and u-velocity of fluid, while v-velocity of fluid is treated as zero:

$$\partial u/\partial r|_+ = 0, \quad r|_+ = 0, \quad \partial T_f/\partial r|_+ = 0, \quad \partial T_s/\partial r|_+ = 0 \tag{15}$$

Table 1
Different models of the fluid to solid interstitial heat transfer coefficient.

Model #	h_v	Ref.
IC-1	$\frac{6(1-\varepsilon)}{d_p}\left[\frac{d_p}{(0.255/\varepsilon)\text{Pr}^{1/3}\text{Re}_p^{2/3}k_f} + \frac{d_p}{10k_s}\right]^{-1}$, $\text{Re}_p > 100$	[31]
IC-2	$\frac{6(1-\varepsilon)k_f[2+1.1\text{Re}_p^{0.6}\text{Pr}^{1/3}]}{d_p^2}$	[31]
IC-3	$\frac{6(1-\varepsilon)k_f[3.22\text{Re}_p^{1/3}\text{Pr}^{1/3}+0.117\text{Re}_p^{0.8}\text{Pr}^{0.4}]}{d_p^2}$, $\text{Re}_p > 40$	[21]
IC-4	$\frac{6(1-\varepsilon)k_f[2+1.8\text{Re}_p^{1/2}\text{Pr}^{1/3}]}{d_p^2}$	[32]
IC-5	$\frac{6(1-\varepsilon)k_f[(7-10\varepsilon+5\varepsilon^2)(1+0.7\text{Re}_p^{0.2}\text{Pr}^{1/3})+(1.33-2.4\varepsilon+1.2\varepsilon^2)\text{Re}_p^{0.7}\text{Pr}^{1/3}]}{d_p^2}$, $0.35 \leqslant \varepsilon \leqslant 1.0, \ 0 \leqslant \text{Re}_p \leqslant 10^5$	[32]

Table 2
Different models of the effective thermal conductivities of fluid and packed bed.

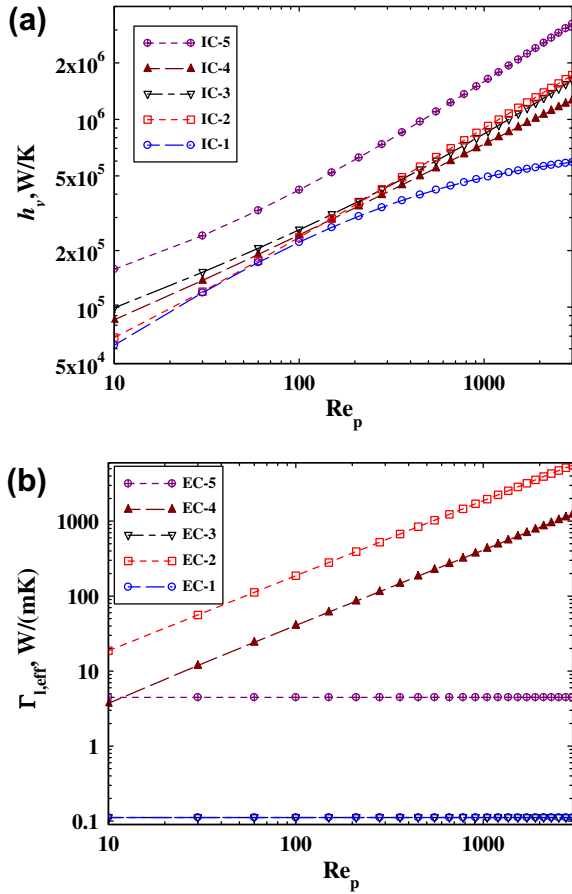| Model #	$\Gamma_{l,eff}$ and $\Gamma_{s,eff}$	Ref.
EC-1	$\Gamma_{l,eff} = \varepsilon k_l$; $\Gamma_{s,eff} = (1-\varepsilon)k_s$	[31]
EC-2	$\Gamma_{l,eff} = \begin{cases} 0.7\varepsilon k_l, & \text{Re}_p < 0.8 \\ 0.5\text{Pr}\text{Re}_p k_l, & \text{Re}_p > 0.8 \end{cases}$; $\Gamma_{s,eff} = \Gamma_{all,eff} - \Gamma_{l,eff}$ where $\Gamma_{all,eff} = k_l(k_s/k_l)^m + 0.5k_l\text{Pr}\text{Re}_p$, $m = 0.28 - 0.757\log\varepsilon - 0.057\log(k_s/k_l)$	[21]
EC-3	$\Gamma_{l,eff} = \varepsilon k_l$; $\Gamma_{s,eff} = k_s\left(\frac{3(1-\varepsilon^2)}{3.6\times10^{10}}\frac{59.8d_p}{2}\right)^{1/3}\frac{1}{0.531d_p} + k_f\left[1 - \sqrt{1-\varepsilon} + \frac{2\sqrt{1-\varepsilon}}{1-\kappa\beta}\left[\frac{(1-\kappa)\beta}{(1-\kappa\beta)^2}\ln\left(\frac{1}{\kappa\beta}\right) - \frac{\beta+1}{2} - \frac{\beta-1}{1-\kappa\beta}\right]\right]$ where $\kappa = k_l/k_s$; $\beta = 1.25((1-\varepsilon)/\varepsilon)^{10/9}$	[32]
EC-4	$\Gamma_{l,eff} = \rho c_{p,l}|\vec{u}|d_p\left(\frac{0.73}{\text{Re}_p\text{Pr}} + \frac{0.5}{1+\frac{9.7}{\text{Re}_p\text{Pr}}}\right)$; $\Gamma_{s,eff} = k_f\left[1 - \sqrt{1-\varepsilon} + \frac{2\sqrt{1-\varepsilon}}{1-\kappa\beta}\left[\frac{(1-\kappa)\beta}{(1-\kappa\beta)^2}\ln\left(\frac{1}{\kappa\beta}\right) - \frac{\beta+1}{2} - \frac{\beta-1}{1-\kappa\beta}\right]\right]$ where $\kappa = k_l/k_s$; $\beta = 1.25((1-\varepsilon)/\varepsilon)^{10/9}$	[20]
EC-5	$\Gamma_{l,eff} = k_l\frac{1+2\beta\phi+(2\beta^3-0.1\beta)\phi^2+\phi^3 0.05\exp(4.5\beta)}{1-\beta\phi}$; $\Gamma_{s,eff} = 0$ where $\phi = 1 - \varepsilon$, $\beta = \frac{k_s-k_l}{k_s+2k_l}$	[28]

Fig. 2. Variations in the (a) interstitial heat transfer coefficient, and (b) effective thermal conductivity of fluid, with the Reynolds number.

2.3.1.4. BC 4 ($0 \leqslant x \leqslant H$, $r = D/2 + l_{in1} + l_{st} + l_{in2}$). This boundary represents the outmost surface of the storage tank exposing to the ambient air. At this boundary, heat transport between the surface and the ambient air are through forced convection. Thus the following boundary condition is specified:

$$-k_{in2} \frac{\partial T}{\partial r}\bigg|_{-} = h(T_{in2} - T_{\infty}) \qquad (16)$$

The heat transfer coefficient h is taken from the forced convection correlation for laminar incompressible flow over a flat surface [33]:

$$\mathrm{Nu} = hH/k = 0.664 \mathrm{Re}_D^{1/2} \mathrm{Pr}^{1/2}, \quad \mathrm{Re}_D = \frac{u_{air} D}{v_{air}} \qquad (17)$$

where u_{air} and v_{air} are the velocity and viscosity of ambient air, respectively.

2.3.1.5. BC 5 ($x = 0$ or $x = H$, $D/2 \leqslant r \leqslant D/2 + l_{in1} + l_{st} + l_{in2}$). These boundaries represent the two cross sections of the insulation layers and tank steel wall adjacency to the fluid inlet and outlet, at which adiabatic conditions are assumed:

$$\partial T_{in1}/\partial x = \partial T_{st}/\partial x = \partial T_{in2}/\partial x = 0 \qquad (18)$$

2.3.1.6. BC 6 ($0 \leqslant x \leqslant H$, $r = D/2$). This interface represents the inner surface of the insulation layer 1 contacting the molten salt and the solid fillers, at which non-slip boundary is used for the fluid flow

and energy balance is satisfied for heat transfer between the molten salt and the insulation layer. While for the temperature of solid fillers, adiabatic boundary is assumed

$$u|_{-} = v|_{-} = 0; \Gamma_{f,eff}|_{-} \frac{\partial T_f}{\partial r}\bigg|_{-} = \Gamma_{in1}|_{-} \frac{\partial T_{in1}}{\partial r}\bigg|_{+}; \ \Gamma_{s,eff}|_{-} \frac{\partial T_s}{\partial r}\bigg|_{-} = 0 \qquad (19)$$

2.3.2. Initial conditions

During the discharging process, cold molten salt is pushed to the tank through the bottom port with a fixed temperature and velocity. At the beginning of the discharging process, it is assumed that the tank is filled with molten salt and solid fillers which have the same hot temperature, and the tank wall is in thermally equilibrium with the interior hot storage material and the outside ambient air with a velocity of 5 m s^{-1}. To get that kind of initial conditions, the codes are first run for the tank with an initial uniform hot temperature of T_h throughout the whole computational domain (including the wall regions) and a fixed molten salt velocity (u_{in}) in the storage region. During the running, the molten salt temperature at the inlet port is also fixed at T_h. When the distribution of wall temperature reaches to a steady state, the results of temperature field and velocity field are used as the initial temperature and velocity conditions for the discharging process.

2.4. Numerical method

The above described governing equations were numerically solved using the finite volume method described by Patankar. The stability-guaranteed second-order difference (SGSD) scheme [34] was used for the convective fluxes, while the central-differencing scheme was used for discretizing the diffusion fluxes. The pressure–velocity coupling is treated with the SIMPLER (Semi-Implicit Method for Pressure-Linked Equations Revised) algorithm. For time discretization, a fully implicit scheme is used with a constant time step. The above mentioned numerical method has been implemented in a self-written simulation code which was developed to resolve the coupled non-linear and time dependent governing equations for the packed-bed thermocline system. After the grid and time-step independence check, a non-uniform grid and a time step of 5 s are employed. The used convergence criteria at each time step are that the residuals for all equations drop below 10^{-4}.

In order to quantify the amount of useful energy that a thermocline storage tank can deliver during the discharging process, the effective discharging efficiency, η, is introduced. It is defined as the ratio between the useful energy that can be recovered from the tank to the maximum energy stored, and can be expressed as:

$$\eta = \frac{\int_0^{t_d} \dot{m} c_{p,f}(T_{f,out} - T_{f,in}) dt}{\text{Total energy initially stored in the thermocline tank}} \qquad (20)$$

where t_d represents the time at which the outlet molten salt temperature drops to a threshold value, i.e., $T_h - 20\,^\circ\mathrm{C}$. The threshold value is determined by the application of interest, and is chosen to be ($T_h - 20\,^\circ\mathrm{C}$) in this work, implying that the thermal energy recovered at temperatures greater than ($T_h - 20\,^\circ\mathrm{C}$) is considered useful in generating superheated steam for the steam turbine.

3. Results and discussion

3.1. Model validation

This section discusses the model validation by inspecting the difference between the numerically predicted results and the experimentally measured results. The experimental results of Pacheco et al. [26] based on a pilot 2.3 MWh t molten salt thermocline storage system are used to validate the numerical model. The

pilot storage system used a low-cost mixture of quartzite rock and sand as the filler material and solar salt (a mixture of 60 wt.% $NaNO_3$ and 40 wt.% KNO_3) as the heat transfer fluid. The simulation uses the same conditions as in the experiment which are summarized in Table 3. IC-2 and EC-2 are used in the model for the interstitial heat transfer coefficient and the effective thermal conductivity, respectively.

Fig. 3 shows the experimental and numerical results for the axial temperature profiles of molten salt in the storage tank. The numerical results are chosen from the centerline ($0 \leqslant x \leqslant H, r = 0$) of the tank as shown in Fig. 1. One can observe that the experimental results show some scatters, indicating an inherent experimental uncertainties. The observed scatters may also be related to possible vortex of molten salt when flowing through the tank, which needs more sophisticated modeling to validate. Generally, within the experimental uncertainty, the present numerical predictions seem to be in good agreement with the experimental ones.

From Fig. 3, one can also see clearly that there is a thermal gradient, or thermocline, running vertically through the tank. With the increase in the discharging time, the thermocline region moves upward, leaving more cold region at the base part and less hot region at the top part of the tank. Moreover, it is interesting to see that the thermocline region continues to expand with the discharging time, indicated by the reduced slopes of the temperature profiles.

As is known, the maintenance of a thin thermocline in the tank is essential to achieve a high discharging efficiency of the storage system. However, the thermocline behavior may be influenced by many factors. Sensitivity study is carried out in the following sections to better understand the effects of different transport mechanisms on the thermocline behavior by inspecting some dominant influencing factors. The results in the following sections are based on a 50 MWh t hypothetical packed-bed molten salt thermocline
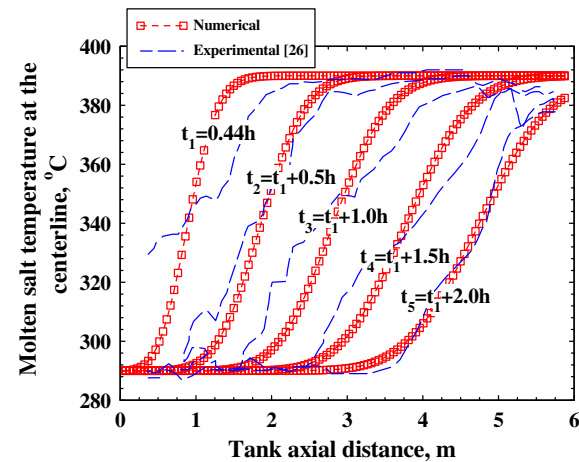

Fig. 3. Comparison between the numerical and experimental thermocline profiles during a discharging cycle of a packed-bed molten-salt thermocline system.

storage system which has a utility-scale geometric parameters as summarized in Table 3.

3.2. General thermal behavior

This section shows the general thermal behavior of a discharging process of the 50 MWh t hypothetical packed-bed thermocline storage system. Fig. 4 shows the two-dimensional distributions of molten salt temperature at different discharging time, i.e., 50, 100, 150, 200, 250 min. One can clearly see that the thermocline region is moving upward with the discharging time, accompanied by slight expansion. More detailed information about the discharging behavior can be revealed by analyzing Figs. 5–7.

Fig. 5 shows the representative temperature distributions of molten salt and solid fillers along the axial direction at different positions inside the tank: the centerline ($0 \leqslant x \leqslant H, r = 0$) and the boundary line ($0 \leqslant x \leqslant H, r = D/2$) as shown in Fig. 1. Since the temperature profiles are varying during the discharging process as shown in Fig. 3, the temperature profile at a specific moment, at which the average temperature of the inlet and outlet temperatures arrives at the middle position of the tank (i.e., $x = H/2$), is chosen as the representative profile. It is clear seen from Fig. 5 that there are three temperature regions within the tank: the cold region, the thermocline region, and the hot region. At the same position, the molten salt temperature is very close to the solid filler temperature: the temperature difference is only about 0.4 °C in the thermocline region and is nearly zero in the hot and cold regions. The very small deviation of molten salt temperature from the solid filler temperature indicates that, with the present parameters and correlations (EC-2 and IC-2), the heat transfer rate between solid and fluid is very fast and the thermal energy stored in the solid fillers can be effectively transferred to the flowing molten salt.

Fig. 5 also compares the temperature profiles at the centerline and the boundary line. It is found that with the present three-layer wall structure, the molten salt temperature near the wall only deviates slightly from that at the central line. The temperature difference between the central region and the boundary region can be more clearly revealed by referring to Fig. 6 which shows the cross-sectional molten salt temperature distributions at different tank heights. It is clear that the cross-sectional molten salt temperature is very uniformly distributed, and there is only a very slight variation near the solid wall. Taking the molten salt temperature at $x = 5$ m as an example, the temperature keeps at 292.5 °C in the central region of the tank (e.g., $0 < r < 3.3$ m), while it slightly in-

Table 3
Geometric parameters and properties used in the model.

| Parameters	Pilot-scale tank for model validation	Hypothetical utility-scale tank
Tank height, m	5.9	14.0
Tank radius, m	1.5	4.3
Diameter of quartzite rock, m	0.01905	0.01905
Porosity	0.22	0.22
Thickness of insulation layer, m	0.2	0.2
Thickness of stainless steel wall, m	0.04	0.04
Temperature of hot molten salt, °C	390	390
Temperature of cold molten salt, °C	290	290
Density of quartzite rock, kg m^{-3}	2500	2500
Density of insulation layer, kg m^{-3}	2000	2000
Density of stainless steel, kg m^{-3}	7800	7800
Specific heat capacity, J kg^{-1} K^{-1}		
For quartzite rock	830	830
For insulation layer	960	960
for stainless steel	470	470
Thermal conductivity, W m^{-1} °C^{-1}		
For quartzite rock,	5.69	5.69
For insulation layer	0.1	0.1
For stainless steel	35.0	35.0
Inlet velocity, m s^{-1}	4.186×10^{-4}	6.017×10^{-4}
Grid size	122×75	82×65
Time step, s	5	5
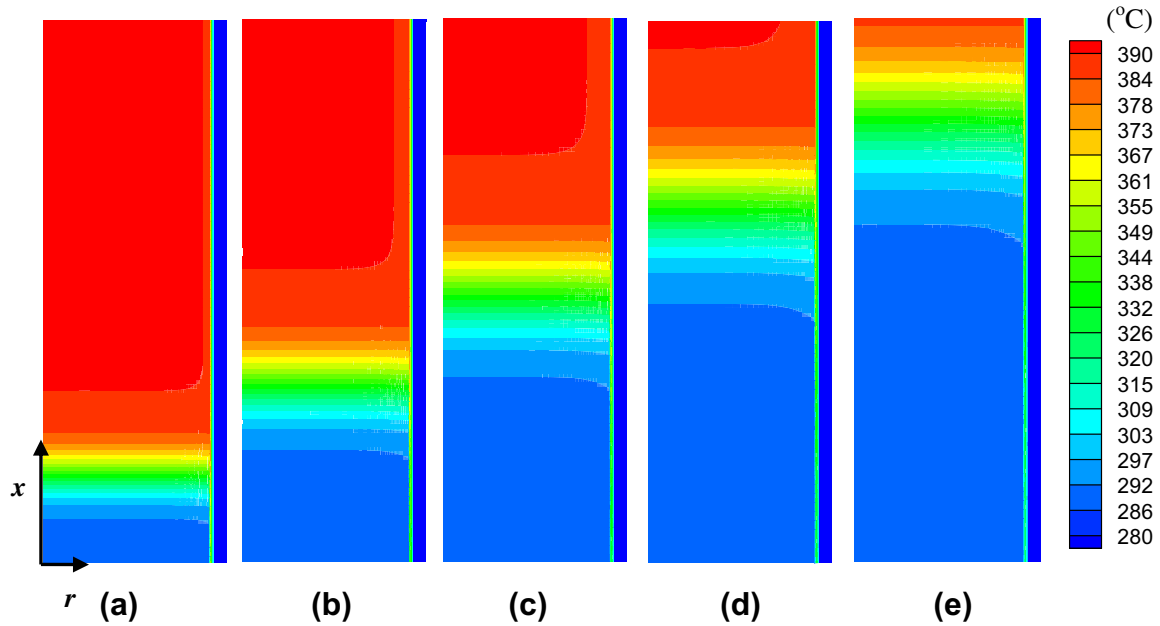
Fig. 4. Two-dimensional distributions of molten salt temperature at different times: (a) 50 min, (b) 100 min, (c) 150 min, (d) 200 min, and (e) 250 min.
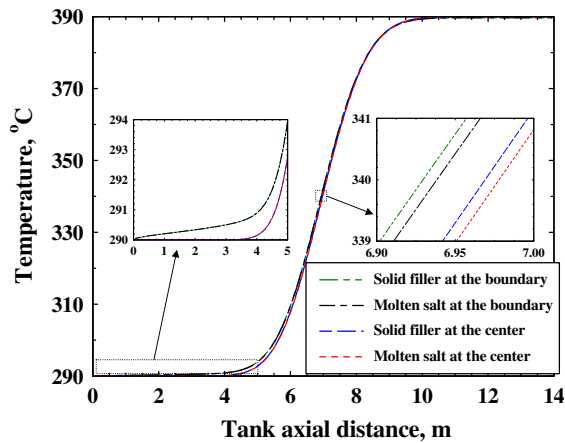

Fig. 5. Representative temperature profiles of molten salt and solid filler at the centerline and the boundary.

Fig. 6. Temperatures of molten salt/insulation and steel layers along the radial direction at various tank heights.

creases to 293.6 °C near the wall (e.g., 3.3 m < r < 4.3 m). The very slight increase in the molten salt temperature near the wall is due to the heating effect of the hot inner insulation layer. Therefore, from Figs. 5 and 6, one can say that a uniform cross-sectional temperature distribution is well achieved with the present insulation structure.

Fig. 7 presents the variations of several parameters with the discharging time including the outlet molten salt temperature, the thermocline thickness, and the ratio of discharged energy to stored energy. For the outlet molten salt temperature, it remains at the hot temperature of 390 °C during the first several hours' discharging and starts to decline after about 3.8 h. That is because with the moving-up of thermocline region during the discharging, the hot region shrinks continuously. When the thermocline region arrives at the outlet, the hot region disappears and the outlet molten salt temperature starts to decrease. After about 6.6 h discharging, the outlet molten salt temperature approaches 290 °C, indicating that the tank is occupied by cold molten salt and solid fillers and the stored energy is fully discharged. It should be pointed out that after about 4.6 h, the outlet molten salt temperature falls below the
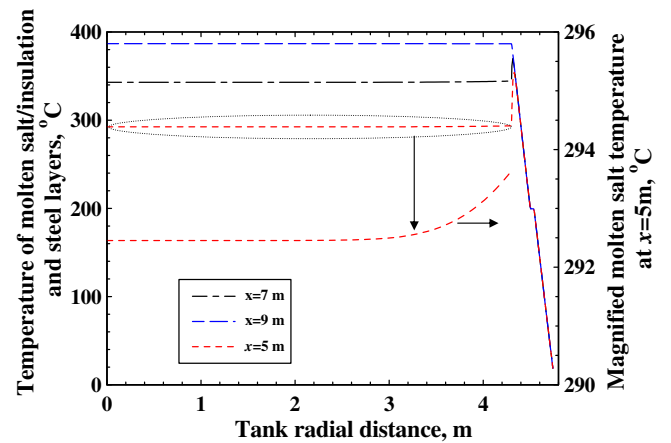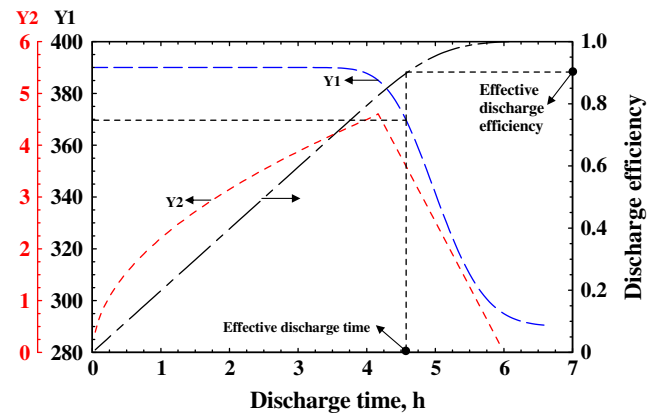

Fig. 7. Variations in the molten salt temperature at the outlet (Y1, °C), thermocline thickness (Y2, m), and discharge efficiency, with the discharging time.

threshold value (i.e., 370 °C) and the following discharged thermal energy cannot be utilized for useful steam generation.

For the corresponding ratio of discharged energy to stored energy, it increased first linearly until the thermocline region arrives at the outlet ($\sim$3.8 h), and then the increase becomes slow. After the stored thermal energy is fully discharged ($\sim$6.6 h), the ratio approaches 100%. One can clearly see that the effective discharging efficiency is about 90%.

Fig. 7 also includes the variation in the thermocline thickness, which is defined as the covering length of the thermocline region and can be expressed as:

$$L_{tc} = \begin{cases} H(T_{crit,h}) - H(T_{crit,l}), & (T_{s,in} \leqslant T_{crit,l}) \& (T_{s,out} \geqslant T_{crit,h}) \\ H(T_{crit,h}) - 0, & T_{s,in} > T_{crit,l} \\ H - H(T_{crit,l}), & T_{s,out} < T_{crit,h} \end{cases}$$

(21)

where $T_{crit,l}$ and $T_{crit,h}$ represent the critical low and hot temperatures for evaluating the thermocline thickness, respectively, and $T_{s,in}$ and $T_{s,out}$ are the solid filler temperatures at the inlet and outlet. $T_{crit,l}$ and $T_{crit,h}$ are chosen to be 295 and 385 °C in the present study, respectively. From Fig. 7, the thermocline thickness first increases sharply, and after the cold region appears the increase in the thickness becomes slower. The thickness climbs to a maximum value when the thermocline region arrives at the outlet, i.e., 4.6 m at 4.2 h, and then it decreases nearly linearly with the fading of the thermocline region. Therefore, the thermocline region can cover almost one third of the tank height at its largest thickness for this case. The thermocline thickness is an important indicator for the thermal performance of the packed-bed thermocline storage tank, and it will be emphatically analyzed in the following sections.

3.3. Evaluation on the interstitial heat transfer coefficient

In this section, different interstitial heat transfer coefficient correlations, listed in Table 1 and shown in Fig. 2a, are first evaluated by analyzing the numerical results based on the different correlations. Fig. 8 shows the corresponding different representative temperature distributions of molten salt along the axial direction, in which the average temperature of the inlet and outlet temperatures appears at the middle position of the tank. It is seen that the different temperature profiles coincide well with each other, despite that the correlation IC-5 results in a much slightly steeper thermocline region. Fig. 9 presents the different variations in the thermocline thickness during the discharging process, which are almost the same for all the correlations except that the correlation IC-5 leads to a slightly slower increase in the thermocline thickness. The results shown in Figs. 8 and 9 can be explained by referring to the different correlations shown in Fig. 2a. One can see that there are no big differences (usually <30%) in the interstitial heat transfer coefficients predicted by correlations IC-1, 2, 3, and 4. Although correlation IC-5 gives higher values, the differences are generally smaller than three times. Therefore, one can conclude that there will be no big difference in the predicted numerical results using the different interstitial heat transfer correlations shown in Fig. 2a. Since the correlations IC-1, 2, 3, and 4 are very close to each other, one of them (IC-2 in the present work) is arbitrarily used in the following section.

In order to dig into the effect of the interstitial heat transfer coefficient on the thermal behavior of the packed-bed thermocline system, a wide range of interstitial heat transfer coefficients coming from products of the value from IC-2 and different scale factors (i.e., 0.01, 0.1, 1, 10, and 100) are tested. The corresponding different representative temperature distributions of molten salt along the axial direction are shown in Fig. 10. It is seen that increasing the coefficient from the value predicted by IC-2 by 10 times or even
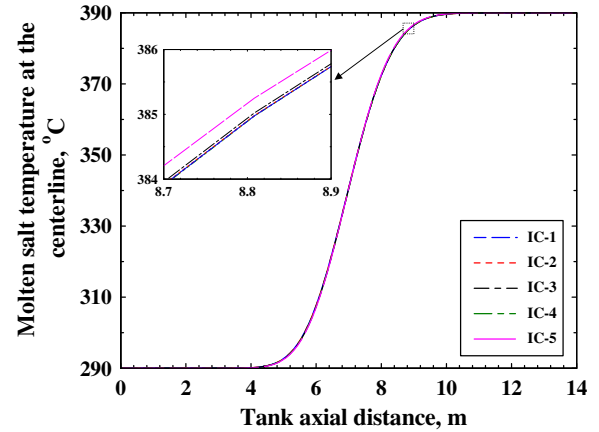

Fig. 8. Representative temperature profiles of molten salt at the centerline using various interstitial heat transfer coefficients.
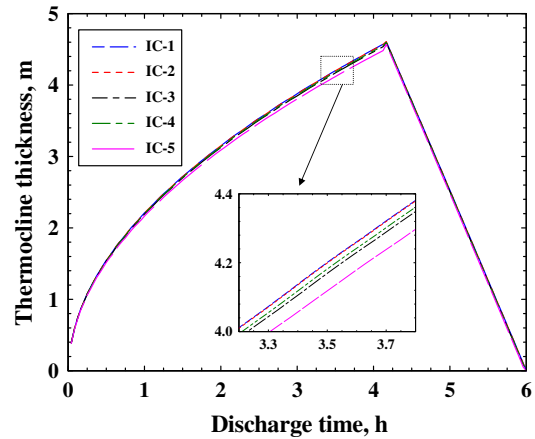

Fig. 9. Variations in the thermocline thickness with the discharging time using various interstitial heat transfer coefficients.

100 times cannot further alter the temperature profile, indicated by the corresponding three overlapped temperature profiles. That means the present interstitial heat transfer coefficient (from IC-2) is large enough to achieve a very fast heat transfer rate between solid fillers and molten salt, which can be reflected by the very small temperature difference between solid fillers and molten salt (<0.4 °C) as shown in Fig. 11.
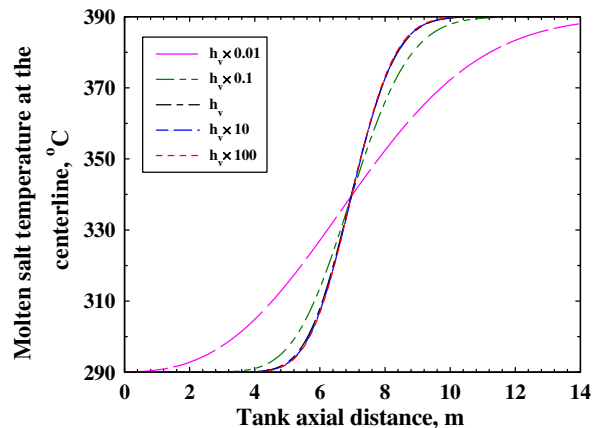

Fig. 10. Representative temperature profiles of molten salt at the centerline using scaled interstitial heat transfer coefficients from IC-2.

On the contrary, decreasing the coefficient from the value predicted by IC-2 results in an evident less steeper temperature gradient, indicating an expanded thermocline region. When the coefficient becomes one hundredth of the value predicted by IC-2, the thermocline region almost occupies the whole tank height. That is because the heat transfer rate between the solid fillers and molten salt is lowered when decreasing the interstitial heat transfer coefficient. As a result, the stored energy in the solid fillers cannot be effectively removed by the fluid and the heat transfer region or thermocline region is extended. The less effective heat transfer can also be reflected by the maximum temperature difference between solid and fluid which is shown in Fig. 11. Decreasing the coefficient leads to a sharp increase in the temperature difference: when the coefficient becomes one hundredth of the value predicted by IC-2, the maximum temperature difference increases sharply from about 0.4 to 11.7 °C.

The effects of the tested interstitial heat transfer coefficients on the variation in the thermocline thickness during the discharging process are presented in Fig. 12. Compared to the result for the coefficient predicted by IC-2, increasing the coefficient leads to negligible changes in the thermocline thickness variation, while decreasing the coefficient results in marked increases in the expanding rate of the thermocline thickness and the maximum value. When the coefficient becomes one hundredth of the value predicted by IC-2, the maximum thermocline thickness is increased significantly from about 4.5 to 10.8 m.

Fig. 13 presents the variations in the outlet molten salt temperature with the discharging time. It is seen that with the decrease in the coefficient, the outlet molten salt temperature starts to decrease earlier and the effective discharging time is shortened. The corresponding effective discharging time and the effective discharging efficiencies are listed in Table 4. For the coefficients equal or larger than the value predicted by IC-2, the effective discharging time and discharging efficiencies are all about 4.57 h and 90.0%, respectively. However, when the coefficient is decreased below the value predicted by IC-2, the effective discharging time and discharging efficiencies are evidently decreased. When the coefficient becomes one hundredth of the value predicted by IC-2, the effective discharging time is decreased from about 4.6 to 3.6 h, and the effective discharging efficiency is significantly decreased from 90% to 70%.

Therefore, from Figs. 9–13, it can be said that the interstitial heat transfer coefficient, or equivalently the heat transfer rate between the solid and fluid, plays a crucial role on the thermal behavior of the packed-bed thermocline storage system. One should

Fig. 12. Variations in the thermocline thickness with the discharging time using scaled interstitial heat transfer coefficients from IC-2.

Fig. 13. Variations in the molten salt temperature at the outlet and discharge efficiency with the discharging time using scaled interstitial heat transfer coefficients from IC-2.
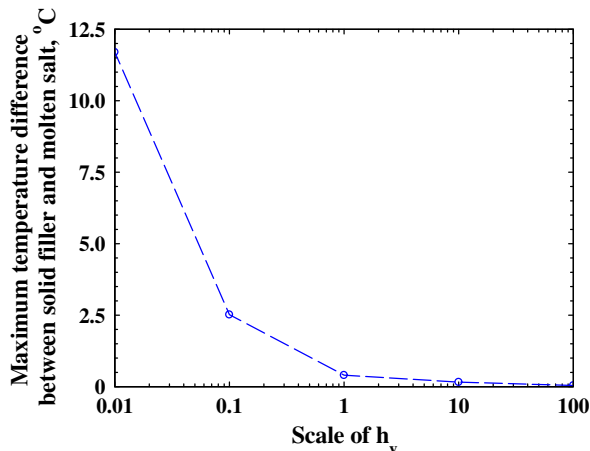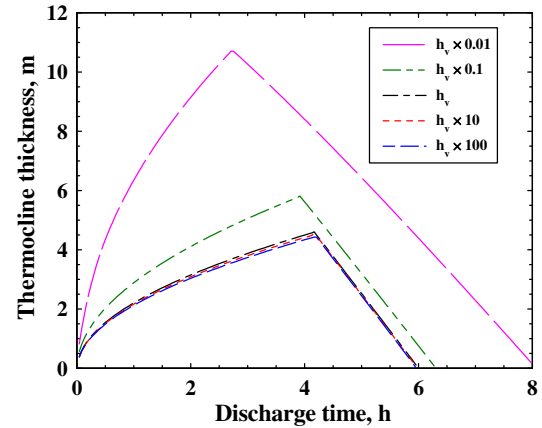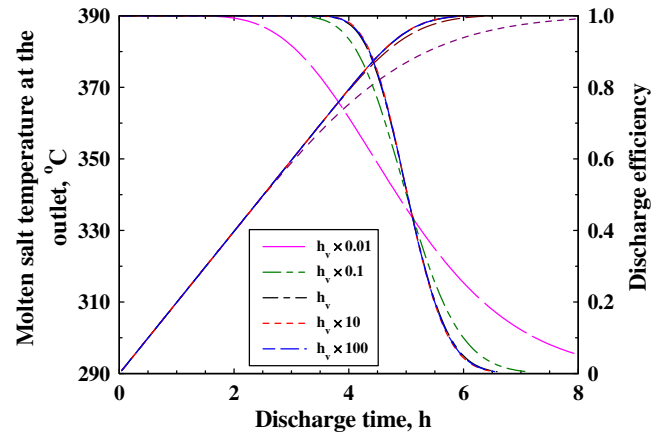

Fig. 11. Variations in the maximum temperature differences between solid filler and molten salt with the scale of the interstitial heat transfer coefficient from IC-2.

Table 4
Effective discharging time and discharging efficiencies for various conditions.

Conditions	Effective discharge time ($\geqslant 370$ °C), h	Effective discharge efficiency ($\geqslant 370$ °C), %
h_v (IC-2) × 0.01	3.625	69.61
h_v (IC-2) × 0.1	4.417	86.40
h_v (IC-2)	4.568	89.54
h_v (IC-2) × 10	4.578	89.78
h_v (IC-2) × 100	4.580	90.03
Solid thermal conductivity: 0 W m^{-1} °C^{-1}	4.576	89.88
Solid thermal conductivity: 5 W m^{-1} °C^{-1}	4.568	89.70
Solid thermal conductivity: 25 W m^{-1} °C^{-1}	4.544	89.17
Solid thermal conductivity: 100 W m^{-1} °C^{-1}	4.457	87.3
Solid thermal conductivity: 400 W m^{-1} °C^{-1}	4.196	81.7

achieve a large enough coefficient in the storage system by optimizing the filler properties, etc., so that effective thermal storage and discharge can be realized.

3.4. Evaluation on the effective thermal conductivity

In this section, different effective thermal conductivity correlations listed in Table 2 and shown in Fig. 2b are evaluated at first. Fig. 14 presents the corresponding different representative temperature distributions of molten salt along the axial direction. It can be seen that the temperature profiles predicted by the correlations EC-1, 3, 4, and 5 agree well with each other, and the profiles predicted by the correlation EC-2 deviates very slightly from the others. Fig. 15 shows the different variations in the thermocline thickness during the discharging process. Also, the variations in the thermocline thickness are almost the same for all the correlations except that the correlation EC-2 leads to a little higher increase in the thermocline thickness.

The above results shown in Figs. 14 and 15 can be explained by follows. As can be seen from Fig. 2b, the predicted effective conductivity of molten salt by EC-2 is much larger than the others, and the predicted effective conductivity of solid fillers by EC-2 (e.g., 11.43 W (mK)$^{-1}$) is also larger than the others (e.g., 4.44, 3.13, 2.93, and 0 W (mK)$^{-1}$). Higher effective thermal conductivities of fluid and solid enhance the thermal diffusion, and thus lead
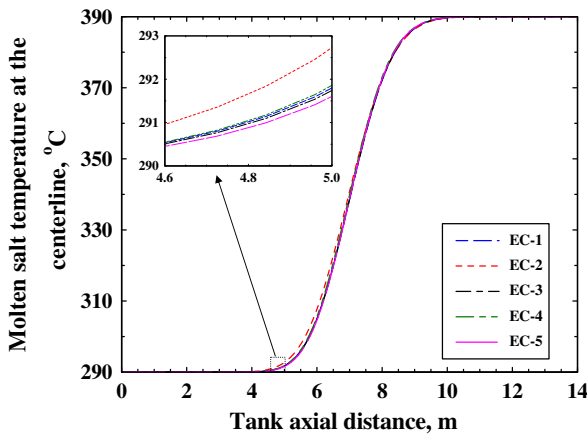

Fig. 14. Representative temperature profiles of molten salt at the centerline using various effective thermal conductivities.
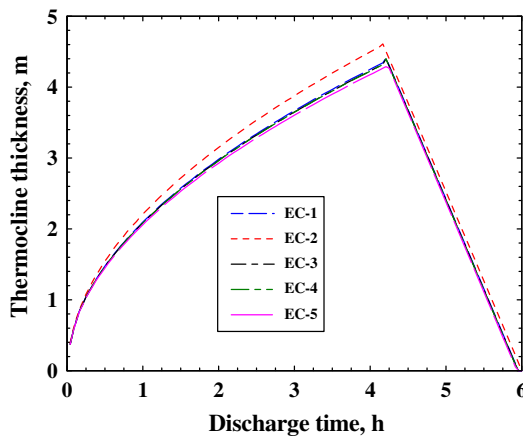

Fig. 15. Variations in the thermocline thickness with the discharging time using various effective thermal conductivities.
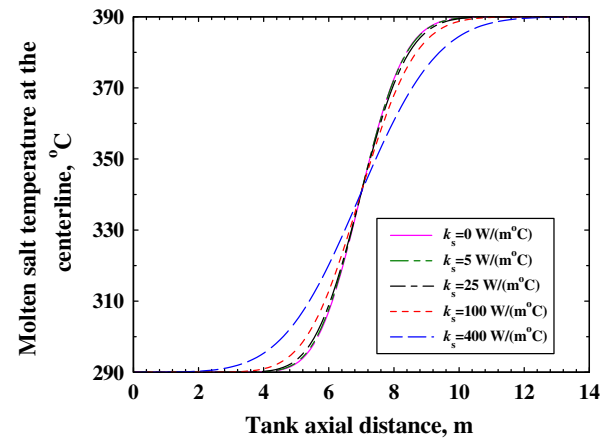

Fig. 16. Representative temperature profiles of molten salt at the centerline using IC-2 and EC-2 with different thermal conductivities of solid filler.

to an expanded thermocline region. Generally, one can see that there will be no big difference in the predicted numerical results using EC-1, 3, 4, and 5, and a very little thicker thermocline region can be predicted using EC-2 which is arbitrarily used in the follows.

The effect of thermal conductivity of solid fillers is also investigated based on the EC-2 correlation. Various values of solid thermal conductivity, e.g., 0, 5, 25, 100, and 400 W (mK)$^{-1}$, are tested. The corresponding different representative temperature distributions of molten salt along the axial direction and the variation in the thermocline thickness during the discharging process are shown in Figs. 16 and 17, respectively. It is seen that increasing the thermal conductivity from 0 to 400 W (mK)$^{-1}$ leads to a less steeper temperature gradient, or an increase in the maximum thermocline thickness (e.g., from 4.5 to 7.5 m). Accordingly, there are also some changes in the corresponding effective discharging times and effective discharging efficiencies which are also listed in Table 4. With the increase in the solid thermal conductivity from 0 to 400 W (mK)$^{-1}$, the effective discharging time is decreased from about 4.58 to 4.20 h and the discharging efficiency is decreased from 89.9% to 81.7%. These findings indicate that solid filler materials with lower thermal conductivities are preferred for this kind of the packed-bed molten salt thermocline thermal storage system. It should also be noted that materials with very high conductivities are typically pure metals which are not feasible in a real thermocline tank due to cost constraints. Rock materials are expected in a real tank due to its low cost and its low conductivity.
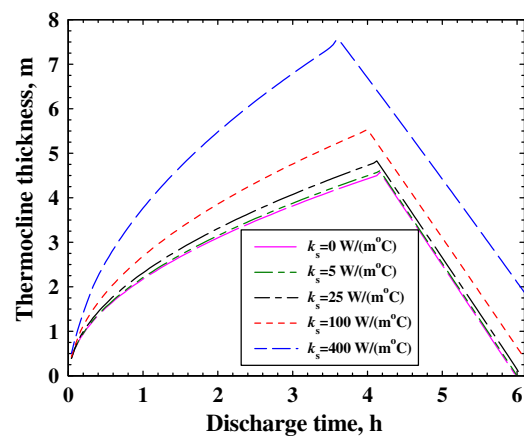

Fig. 17. Variations in the thermocline thickness with the discharging time using IC-2 and EC-2 with different thermal conductivities of solid filler.

4. Conclusions

In this study, a comprehensive transient, two-dimensional, two-phase model for the packed-bed molten salt thermocline system is presented to investigate the thermal performance of the system. The model is first validated based on the experimental results in the literature, and then it is used to numerically study the discharging process of the packed-bed thermocline system. Various numerical results are examined, including the two-dimensional temperature distributions of molten salt, the variations in the outlet molten salt temperature and the thermocline thickness with the discharging time, the representative thermocline profiles, the effective discharging time and the effective discharging efficiency, etc. Salient findings from this study are summarized as follows:

(a) The thermocline region is moving upward during the discharging process with slight expansion. With the tank height of 14 m, the thermocline region can cover more than one third of the whole tank at its maximum thickness.

(b) With the help of two insulation layers, a uniform cross-sectional temperature distribution within the tank can be achieved, although the molten salt near the wall can be slightly influenced by the wall temperature.

(c) The use of different correlations for the interstitial heat transfer coefficient or the effective thermal conductivity from the literature results in negligible difference in the predicted thermal performance. It is further found that decreasing the interstitial heat transfer coefficient by one hundredth, or increasing the thermal conductivity of solid fillers from 0 to 400 W m^{-1} °C^{-1}, can effectively increase the maximum thermocline thickness, which finally decreases the effective discharging time and the effective discharging efficiency.

Acknowledgements

References

[1] Wang ZF. Prospectives for China's solar thermal power technology development. Energy 2010;35:4417–20.

[2] Yao ZH, Wang ZF, Lu ZW, Wei XD. Modeling and simulation of the pioneer 1 MW solar thermal central receiver system in China. Renew Energy 2009;34:2437–46.

[3] Jin HG, Sui J, Hong H, Wang ZF, Zheng DX, Hou Z. Prototype of middle-temperature solar receiver/reactor with parabolic trough concentrator. J Solar Energy Eng 2007;129:378–81.

[4] He YL, Xiao J, Cheng ZD, Tao YB, MCRT A, VM F, et al. A MCRT and FVM coupled simulation method for energy conversion process in parabolic trough solar collector. Renew Energy 2010;36:976–85.

[5] Yang ML, Yang XX, Yang XP, Ding J. Heat transfer enhancement and performance of the molten salt receiver of a solar power tower. Appl Energy 2010;87:2808–11.

[6] Solar thermocline storage systems: preliminary design study. EPRI, Palo Alto, CA; 2010. p. 1019581.

[7] Gil A, Medrano M, Martorell I, Lázaro A, Dolado P, Zalba B, et al. State of the art on high temperature thermal energy storage for power generation. Part I-Concepts, materials and modellization. Renew Sustain Energy Rev 2010;14:31–55.

[8] Medrano M, Gil A, Martorell I, Potau X, Cabeza LF. State of the art on high temperature thermal energy storage for power generation. Part I-Case studies. Renew Sustain Energy Rev 2010;14:56–72.

[9] Gabbrielli R, Zamparelli C. Optimal design of a molten salt thermal storage tank for parabolic trough solar power plants. J Solar Energy Eng 2009;131:041001.

[10] Kolb GJ, Hassani V. Performance analysis of thermocline energy storage proposed for the 1 MW Saguaro solar trough plant. In: Proceedings of ISEC 2006 ASME international solar energy conference. Denver, CO; 2006.

[11] Pacheco JE, Showalter SK, Kolb WJ. Development of a molten-salt thermocline thermal storage system for parabolic trough plants. In: Proceedings of solar forum 2001 solar energy: the power to choose. Washington, DC; 2001.

[12] Survey of thermal storage for parabolic trough power plants. NREL, Golden, CO; 2000. NREL/SR-550-27925.

[13] Laing D, Lehmann D, Fib M, Bahl C. Test results of concrete thermal energy storage for parabolic trough power plants. J Solar Energy Eng 2009;131:041007.

[14] Brosseau D, Kelton JW, Ray D, Edgar M, Chisman K, Emms B. Testing of thermocline filler materials and molten-salt heat transfer fluids for thermal energy storage systems in parabolic trough power plants. J Solar Energy Eng 2005;127:109–16.

[15] Zuo Y, Li X. Scheme and experiments of a molten-salt hybrid thermocline thermal storage system. Chem Indust Eng Progr 2007;26:1018–22.

[16] Rosen MA, Tang R, Dincer I. Effect of stratification on energy and exergy capacities in thermal storage systems. Int J Energy Res 2004;28:177–93.

[17] Panthalookaran V, Heidemann W, Muller-Steinhagen H. A new method of characterization for stratified thermal energy stores. Solar Energy 2007;81:1043–54.

[18] Haller MY, Cruickshank CA, Streicher W, Harrison SJ, Andersen E, Furbo S. Methods to determine stratification efficiency of thermal energy storage process-review and theoretical comparison. Solar Energy 2009;83:1847–60.

[19] Haller MY, Yazdanshenas E, Andersen E, Bales C, Streicher W, Furbo S. A method to determine stratification efficiency of thermal energy storage process independently from storage heat losses. Solar Energy 2010;84:997–1007.

[20] S.M. Tailor, Mathematical modeling of heat transfer in packed beds with two phase flow. A Thesis in Chemical Engineering of Texas Tech. University; 1981.

[21] Ismail KAR, Stuginsky Jr R. A parametric study on possible fixed bed models for PCM and sensible heat storage. Appl Therm Eng 1999;19:757–88.

[22] Mawire A, McPherson M. Experimental and simulated temperature distribution of an oil-pebble bed thermal energy storage system with a variable heat source. Appl Therm Eng 2009;29:1086–95.

[23] Adeyanju AA. Performance characterization of packed bed storage system. J Eng Appl Sci 2009;4:96–9.

[24] Mawire A, McPherson M, van den Heetkamp RRJ, Mlatho SJP. Simulated performance of storage materials for pebble bed thermal energy storage (TES) systems. Appl Energy 2009;86:1246–52.

[25] Lew JTV, Li P, Chan CL, Karaki W, Stephens J. Transient heat delivery and storage process in a thermocline heat storage system. In: Proceeding of the ASME 2009 international mechanical engineering congress & exposition. Florida, USA.

[26] Pacheco JE, Showalter SK, Kolb WJ. Development of a molten-salt thermocline thermal storage system for parabolic trough plants. J Solar Energy Eng 2002;124:153–9.

[27] Yang Z, Garimella SV. Molten-salt thermal energy storage in thermocline under different environmental boundary conditions. Appl Energy 2010;87:3322–9.

[28] Yang Z, Garimella SV. Thermal analysis of solar thermal energy storage in a molten-salt thermocline. Solar Energy 2010;84:974–85.

[29] Flueckiger S, Yang Z, Garimella SV. An integrated thermal and mechanical investigation of molten-salt thermocline energy storage. Appl Energy 2011;88:2098–105.

[30] Zavoico AB. Solar power tower design basis document. Sandia National Laboratories. Report no. SAND2001-2100; 2001.

[31] Alazmi B, Vafai K. Analysis of variants within the porous media transport models. J Heat Trans 2000;122:303–26.

[32] Visser Coert J. Modelling heat and mass flow through packed pebble beds: a heterogeneous volume-averaged approach. Master's Dissertation. University of Pretoria; 2007.

[33] Lienhard IV J, Lienhard V J. A heat transfer textbook, 3rd ed. Cambridge: Phlogiston Press; 2008.

[34] Li Z, Tao W. A new stability guaranteed second order difference scheme. Numer Heat Trans Part B 2002;42:349–65.